Physics-based model of wildfire propagation towards faster-than-real-time simulations

Paolo Grasso, Mauro S. Innocente

Autonomous Vehicles & Artificial Intelligence Laboratory (AVAILab), Research Institute for Future Transport and Cities, Coventry University, Coventry, UK.

Abstract

This paper presents the mathematical formulation, numerical solution, calibration and testing of a physics-based model of wildfire propagation aimed at faster-than-real-time simulations. Despite a number of simplifying assumptions, the model is comprehensive enough to capture the major phenomena that govern the behaviour of a real fire –namely the pyrolysation of wood; the combustion of a mono-phase medium composed of premixed gas of fuel and air; and the heat transferred by conduction, convection, radiation, mass diffusion and transport due to atmospheric wind. The model consists of a system of coupled partial differential equations, one ensuring the balance of enthalpy, and a set of equations representing the mass formation of each chemical species involved in the combustion. Dimensionality reduction is sought by modelling these three-dimensional phenomena in a two-dimensional space, which has been achieved by means of heat-sources and heat-sinks to account for the third dimension in the energy balance equation. Once calibrated with a widely used non-physics-based commercial wildfire simulator, the proposed **Fire Pro**pagation **M**odel for **F**ast simulations (FireProM-F) is tested, returning similar predictions in terms of the size and shape of the burnt area although similarity deteriorates for windy conditions. FireProM-F has the added benefit of being both physics-based and computationally inexpensive so that its interaction with fire suppressants may also be modelled in the future and simulated in real time.

Keywords: fire spread, forest fire, combustion, calibration, FARSITE simulator.

1. Introduction

Modelling the propagation of wildfires is an incredibly challenging endeavour because of the complexity that arises from its multiphysics and multiscale nature. According to what phenomena, scales and modelling technique are considered, various classifications of wildfire mathematical models are possible (e.g. [1; 2; 3; 4; 5]).

Following the criteria set out in [5] and shown in Fig. 1, a general classification is given by distinguishing between *data-driven*, *theoretical*, and *mechanistic surrogate* models. Data-driven models are built so as to fit available data, theoretical models are mechanistic and based

Email addresses: grassop@uni.coventry.ac.uk (Paolo Grasso), Mauro.S.Innocente@gmail.com (Mauro S. Innocente)

Please cite this article as:
P. Grasso and M.S. Innocente, *Physics-based model of wildfire propagation towards faster-than-real-time simulations*, Computers and Mathematics with Applications 80 (2020) 790–808
https://doi.org/10.1016/j.camwa.2020.05.009

Nomenclature

χ	convective heat transfer coefficient	A_{ref}	reference burnt area
δ_{x}	horizontal optical thickness	c_{h}	enthalpy correction coefficient
δ_{z}	vertical optical thickness	c_{p}	heat capacity coefficient at constant pressure
ϵ	percentage error	c_{w}	wind reduction coefficient
κ	thermal conductivity of gas mixture	e	total specific energy
$\mathbf{q}$	heat flux	h	specific enthalpy
$\mathbf{u}$	velocity vector	H_{u}	moisture fraction
ρ	gas mixture density	M	molar mass of gas mixture
σ	Stefan-Boltzmann constant	M_j	molar mass of jth chemical species
A_{r}	Arrhenius pre-exponential factor	r	reaction rate
H_j	formation enthalpy of jth chemical species at T_{ref}	T	temperature
θ_j	stoichiometric coefficient of jth chemical species	t	time
Δt	time discretisation	T_{amb}	ambient temperature
$\Delta x, \Delta y$	spatial discretisation	T_{a}	activation temperature
ε	radiative emissivity	T_{ig}	ignition temperature
$\widehat{\Delta X}$	downwind fire-front run	T_{ref}	reference temperature
A_{b}	burnt area	X_j	molar fraction of jth species
		X_{e}	extinction molar fraction of fuel

on governing laws directly associated with the phenomena or system being represented, whilst mechanistic surrogate models are based on a few leading assumptions that act as governing laws seemingly unrelated to the problem in question despite making sufficiently accurate predictions. A model in any of these classes may present continuous or discrete variables, responses or structures; and may be deterministic or include some stochasticity to account for uncertainty.

Data-driven models which are purely data-fitting are called black-box models, a.k.a. phenomenological or empirical models. At the other end of the spectrum, theoretical models derived purely from first principles are referred to as white-box models. The combination of governing laws and empirical data results in grey-box models, which are semi-empirical. The latter are considered theoretical if mostly based on governing laws with some parameters calibrated using

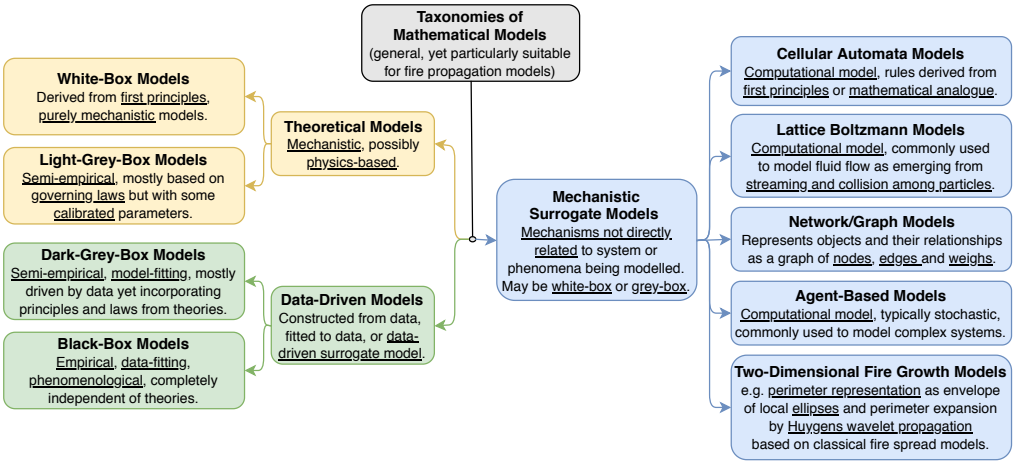

Figure 1: Taxonomies of mathematical models suitable for family of wildfire propagation models (modified from [5]).

empirical data (light-grey-box), whereas they are considered data-driven if mostly driven by data but built upon a predefined structure derived from associated theories (dark-grey-box).

Early models of wildfire propagation consisted of one-dimensional models of fire behaviour based on the empirical determination of key characteristics such as the local rate of spread (RoS) at the headfire or the height and angle of the flames. Based on a heat balance model and empirical data, a prominent example is Rothermel's model [6] which predicts the RoS in the direction of the wind in an environment specified by fuel, weather and topography descriptors [1]. The model was incorporated into the point-based fire modelling system BehavePlus [7] and the Fire Area Simulator FARSITE [8]. For further reading on this type of models, refer to [1; 3; 9; 5].

Theoretical models are typically physics-based, including balances of mass, momentum and energy with mathematical formulations expressed as systems of coupled partial differential equations (PDEs). Physics-based white-box models are often three-dimensional (3D), and attempt to describe all relevant phenomena with model parameters aimed to be mathematically derived. The scale of the model must be finer than the smaller representative scale of the modelled dynamics. In the context of fire modelling, they typically solve convection-reaction-diffusion-radiation equations. Whilst 3D multi-domain, multiscale and multiphase models of wildfire propagation can be found in the literature (e.g. [10; 11; 12; 13; 14]), they are computationally intensive. Physics-based light-grey-box models tend to be two-dimensional (2D), based on simple laws such as energy balance (e.g. [15; 16; 17]), often requiring empirical parameters and experimental data for their calibration to particular conditions. This paper focuses on this type of 2D models. Thus, Ferragut et al. [15] propose a system of two coupled PDEs, one for the energy balance and the other for the convection model. The energy balance is as in Eq. (1), where the energy (e) is an element of a multivalued operator that considers the latent heat of evaporation and the pyrolysis heat, whilst $S(T, X_{\text{fuel}})$ is a source term that accounts for combustion and non-local radiation. Transport due to wind, conduction and convection are also considered. The two main variables are temperature (T) and fuel mass fraction (X_{fuel}).

$$\frac{\partial e}{\partial t} + \overbrace{u \cdot \nabla e}^{\text{transport}} - \overbrace{\nabla(\kappa(T)\nabla T)}^{\text{conduction}} + \overbrace{\alpha T}^{\text{convection}} = \overbrace{S(T, X_{\text{fuel}})}^{\text{source}}, \quad (1)$$

Similarly, Margerit, Séro-Guillaume et al. [16; 18] propose a 2D anisotropic propagation model consisting of only one energy balance equation, as shown in Eq. (2):

$$(1-\Phi)\rho(c_{\text{s}} + H_{\text{u}}c_{\text{l}})\frac{\partial T}{\partial t} = \overbrace{\nabla \cdot (\kappa \nabla T)}^{\text{conduction}} + R_c + \overbrace{\chi(T_{\text{a}} - T)}^{\text{convection}} + \overbrace{(1-\Phi)\rho L_{\text{ev}}\delta_{T=T_{\text{ev}}}\frac{\partial H_{\text{u}}}{\partial t}}^{\text{evaporation}} + M_{\text{r}} \quad (2)$$

where R_c is the combustion heat source, Φ is the porosity of the medium, and c_{s}, c_{l} are the heat capacities of the solid and liquid parts, respectively. Interestingly, the local self-radiation heat flux is neglected while the non-local radiative term (M_{r}) is considered. M_{r} is the integral of all radiation coming from the flame above the simulation domain. The heat loss due to evaporation of a moisture fraction (H_{u}) is considered via the latent heat (L_{ev}) triggered by the evaporation temperature (T_{ev}), where δ is the Dirac distribution.

Mechanistic surrogate models are those designed disregarding the theories that underlie the system or phenomena being modelled, yet based on a few leading assumptions which may be somewhat physics-based [5]. Examples are Cellular Automata (CA) models, Lattice Boltzmann models (LBMs), Network models, and 2D Fire Growth models.

A CA model consists of a system of elements of simple geometry locally connected following a predefined scheme. Two main constituents can be recognised: the *cellular space* and the *transition rule*. The former is a lattice of many identical finite-state machines whereas the transition rule evaluates the new state of the cell taking into account also adjacent cells identified by a *connection scheme*. CA models demonstrate a high level of efficiency and robustness when simulating complex physics. As far as wildfire propagation modelling is concerned, CA are mostly mechanistic surrogates. For instance, the CA model in [19] is not derived from fire dynamics theories but based on some main assumptions which may nonetheless have a physics origin. Other CA-based fire models can be found in [20; 21; 22; 23; 24; 25].

The fundamental idea behind LBMs is a simplification of Boltzmann's representation of fluids as composed of a large but discrete number of particles. This model consists of a discretised representation of the Boltzmann transport equation that relates the particles' distribution to their velocities by means of a *collision operator*. An example is the simulation of combustion in a three-dimensional porous structure in [26].

Another discrete modelling approach, even if rarely adopted, is based on small-world networks. A square lattice is used to model short-range phenomena like radiation, convection and diffusion, whilst fire-spotting processes are described by long-range connections. Two examples are the modelling of initiation of spot-fires due to transport of firebrands [27] and fire-spread onboard naval vessels [28].

Two-Dimensional Fire Growth Models are sometimes referred to as vector-based models. They consist of predicting the fire front line in the form of an envelope curve making use of Huygens' principle [4]. At the core of these models is the notion of the RoS (called R in Rothermel's model), which is the local normal velocity of a fire front. Vector-based models can be further subdivided into two main branches, one using *level sets* and the other based on *markers*.

Level-set-based models (LSMs) such as [29; 30; 31] consist of tracking the interface of the fire front. The 2D curve (ϕ) described in Eq. (3) evolves in time following the rates of spread R_{u} and R_{v} in the x and y directions, respectively.

$$\frac{\mathrm{d}\phi}{\mathrm{d}t} = \frac{\partial\phi}{\partial t} + R_{\mathrm{u}}\frac{\partial\phi}{\partial x} + R_{\mathrm{v}}\frac{\partial\phi}{\partial y} = 0 \tag{3}$$

Marker-based models (MMs) predict the movement of individual points (markers) to be connected to give shape to the fire line. Each marker behaves as a new ignition point for the next time step. The basic propagation geometry is an ellipse focused on the marker, which size, shape and orientation depend on the fuel type, wind intensity and local slope [18; 8]. A major drawback is the need to change the number of markers throughout the simulation to maintain a certain level of precision. Whilst the mathematical formulation of LSMs automatically handles merging fire fronts, MMs need to identify which side delimited by the fire front is the burnt area. Well known vector-based MMs are the Fire Area Simulator FARSITE [8], the Canadian wildland fire growth simulator Prometheus [32] and the Australian Bushfire Risk Management Tool Phoenix [33].

What modelling approach is best at predicting fire behaviour is still an open question, and the subject of much heated debate. For instance, whilst some researchers [34; 3] adamantly support FARSITE given that it has been calibrated to reliably reproduce historical fires, others prefer approaches which are mostly physics-based and reliant on the rigorous description of the underlying fire dynamics. As an example of the latter, the *Fire Dynamics Simulator* (FDS) [35] is the result of 26 years of collaboration between several research centres around the world, FIRETEC [10] has been refined for 22 years, whilst the fire-spread models in [12; 16] have been developed during 16 years of rigorous work by the *Laboratoire d'Energétique et de Mécanique Théorique et Appliquée* (LEMTA). This paper does not intend to answer this *burning* question. Instead, a physics-based approach is adopted as a requirement, since the model is intended to be used to underpin research on innovative firefighting technologies. Therefore, the physics-based interaction between the fire and suppressants will need to be modelled in the future. Nonetheless, the proposed model also attempts to harness the ability of a commercial simulator to predict historical fires by calibrating a few parameters within realistic intervals.

The remainder of this paper is organised as follows: Section 2 presents the mathematical formulation of the proposed model; Section 3 deals with the numerical method implemented to solve the formulated initial boundary value problem; Section 4 is concerned with numerical experiments, where Section 4.1 presents the calibration process, Section 4.2 presents case studies to test the calibrated model, Section 4.3 reproduces a real controlled fire dynamically ignited along an edge, Section 4.4 shows the application of the model to a realistic scenario, and Section 4.5 discusses the results obtained; finally, conclusions are offered in Section 5.

2. Proposed model

In line with [15] and [16], the vegetation stratum is modelled in this paper as a virtual premixed layer of pyrolysis gases and air. The considered reference irreversible chemical reaction is the combustion of methane in air:

$$\theta_1 \mathrm{CH_4} + \theta_2 \mathrm{O_2} \rightarrow \theta_3 \mathrm{CO_2} + \theta_4 \mathrm{H_2O} \tag{4}$$

The reactants in Eq. (4) are the gaseous fuel and oxygen, mixed in air. The latter is considered to be composed of oxygen, carbon dioxide, water vapour, and nitrogen. Even though five chemical species are considered in this model, the nitrogen mass can be assumed constant, therefore leading to only four mass balance equations. The fire spread model can be represented

by a system of five coupled PDEs: Eq. (5) for the enthalpy balance, where F_T is the summation of all heat sources and sinks; and Eq. (6) for the consumption or formation of each of the four chemical species – i.e. fuel, O_2, CO_2 and H_2O.

$$\frac{\partial}{\partial t}\left(c_{\mathrm{p}}T\right) = F_T\left(T, X_i\right) \tag{5}$$

$$\frac{\partial X_i}{\partial t} = F_{X_i}\left(T, X_i\right), \quad i = 1, \ldots, 4 \tag{6}$$

In Eq. (6), F_{X_i} is the molar fraction formation rate. The system of Eqs. (5)–(6) can be expanded as shown in the system of Eqs. (7)–(8).

$$\rho\frac{\partial}{\partial t}\left(c_{\mathrm{p}}T\right) = R_{\mathrm{c}} + Q_{\mathrm{w}} - \nabla\cdot\left(\mathbf{q}_{\mathrm{c}} + \mathbf{q}_{\mathrm{d}} + \mathbf{q}_{\mathrm{r}}\right) + Q_{\mathrm{conv}} + Q_{\mathrm{rz}} \tag{7}$$

$$\frac{\partial X_i}{\partial t} = -\frac{\theta_i}{\theta_1}\frac{M_i}{M_1}r, \tag{8}$$

where the following terms can be identified:

- R_{c}: combustion energy source;
- Q_{w}: transport term due to wind;
- $\mathbf{q}_{\mathrm{c}}$: conductive heat flux;
- $\mathbf{q}_{\mathrm{d}}$: interdiffusional enthalpy flux;
- Q_{conv}: vertical convection heat loss;
- $\mathbf{q}_{\mathrm{r}}$: 2D radiation heat flux;
- Q_{rz}: vertical radiation heat loss.

Notice that the radiation heat flux is split into two contributions: the auto-radiation in the 2D domain, and the emitted radiation outward from the domain in the vertical direction. Thus, the proposed **Fire Pro**pagation **M**odel for **F**ast simulations (FireProM-F) is governed by Eqs. (7)-(8).

2.1. Combustion energy

The combustion energy in Eq. (9) depends on the combustion enthalpy (h_c) and on the reaction rate (r), both of which depend on the temperature (T), the mole fraction of fuel (X_1), and the mole fraction of oxidiser (X_2).

$$R_{\mathrm{c}} = -\rho c_{\mathrm{h}} h_{\mathrm{c}}\frac{M}{M_1}r \tag{9}$$

The role of the enthalpy proportionality coefficient (c_{h}) is explained in Section 4.1. The combustion enthalpy in Eq. (10) consists of the summation of all formation enthalpies H_i at the specific local temperature T. The reference empirical values $H_{i,\mathrm{ref}}$ and T_{ref} can be found in [36].

$$h_{\mathrm{c}} = \frac{H_{\mathrm{c}}\left(T\right)}{\bar{M}} = -\frac{1}{\bar{M}}\sum_{i=1}^{5}\theta_i H_i\left(T\right) = \frac{1}{\bar{M}}\sum_{i=1}^{5}\theta_i\left(H_{i,\mathrm{ref}} + M_i c_{\mathrm{p}i}\left(T_{\mathrm{ref}} - T\right)\right) \tag{10}$$

The combustion rate in Eq. (11) represents the rate of fuel consumption and follows the law of mass action –i.e. the exponential Arrhenius law. The pre-exponential coefficient (A_r) and the activation temperature (T_{a}) are empirical parameters that depend on the fuel structural and chemical properties [37].

$$r = -\delta^{+}_{(T,X_{1,2})} A_r T X_1^{0.5} X_2 \exp\left(-\frac{T_a}{T}\right) \tag{11}$$

In Eq. (11), $\delta^{+}_{(T,X_{1,2})}$ is the Kronecker delta as defined in Eq. (12), which represents a simple extinction model: if the temperature is lower than the ignition temperature (T_{ig}) or if either the fuel mass fraction or the oxidant mass fraction is lower than the corresponding flame extinction value (X_{1e}, X_{2e}), the combustion is deactivated –i.e. the combustion rate is null. It is assumed here that the ignition temperature is equal to the activation temperature.

$$\delta^{+}_{(T,X_{1,2})} = \begin{cases} 1 & \text{if} \quad T > T_{ig} \wedge X_{1,2} > X_{1,2e} \\ 0 & \text{otherwise} \end{cases} \tag{12}$$

2.2. Transport due to wind

The transport term in Eq. (13) models windy conditions, where $\mathbf{u} = (u_1, u_2)$ is the atmospheric wind velocity. The meaning of the wind reduction coefficient (c_w) is explained in Section 4.1.

$$Q_w = -\rho c_w \mathbf{u} \cdot \nabla\left(c_p T\right) \tag{13}$$

2.3. Conductive heat flux

The conductive heat flux is modelled as shown in Eq. (14), where the thermal conductivity (κ) is assumed to be constant.

$$\mathbf{q}_c = -\kappa \nabla T \tag{14}$$

2.4. Interdiffusional enthalpy flux

The adopted interdiffusional enthalpy flux is as in Eq. (16), based on the Fickian approximation of the diffusive mass flux ($\mathbf{J}_i$) shown in Eq. (15) [38]. The diffusivity (D_i) is assumed to be the same for every chemical species and it has been expressed in Eq. (16) as a function of κ to reduce the number of parameters [39].

$$\mathbf{J}_i \approx -\rho\left(D_i \nabla Y_i - Y_i \sum_j D_j \nabla Y_j\right) \tag{15}$$

$$\mathbf{q}_d = \sum_i h_i J_i \approx \sum_i h_i \rho D_i \nabla Y_i \approx \frac{\kappa T}{c_p \bar{M}} \sum_i c_{pi} \nabla\left(X_i M_i\right) \tag{16}$$

2.5. Vertical convection

The heat loss due to vertical convection is governed by the simple formulation in Eq. (17), where the atmospheric domain above the vegetation is at ambient temperature (T_{amb}).

$$Q_{conv} = \chi\left(T_{amb} - T\right) \tag{17}$$

As suggested by Séro-Guillaume et al. [18], this simple linear model should be improved. Nonetheless, one could assume the disregarded nonlinearities in the vertical convection dynamics to be implicitly embedded in the radiation heat loss in Eq. (25). Though this is not a rigorous theoretical observation, it could serve well for the purpose of the proposed wildfire model.

2.6. 2D radiation heat flux

Radiation is a volumetric phenomenon proportional to the 4$^{\text{th}}$ power of the temperature of the source [40]. The hemispherical radiation power ($\mathbf{q}$) emitted by a finite radiative volume is shown in Eq. (18) in terms of the Boltzmann constant (σ), the emittance (ε), and the radiation aspect (ϕ).

$$\mathbf{q} = \sigma\varepsilon\phi T^4 \tag{18}$$

Let us consider two sources separated by the absorption length (δx), which are at different temperatures as in Eq. (19). Then, the radiative heat fluxes, $\mathbf{q}_{\text{A}}$ and $\mathbf{q}_{\text{B}}$, are as in Eq. (20).

$$\begin{cases} T_{\text{A}} = T \\ T_{\text{B}} = T + \frac{\partial T}{\partial x}\delta x \end{cases} \tag{19}$$

$$\begin{cases} \mathbf{q}_{\text{A}} = \sigma\varepsilon\phi T^4 \\ \mathbf{q}_{\text{B}} = \sigma\varepsilon\phi\left(T + \frac{\partial T}{\partial x}\delta x\right)^4 \end{cases} \tag{20}$$

The 4$^{\text{th}}$ power of the temperature at point B in Eq. (20) may be simplified by neglecting some small differentials, as shown in Eq. (21).

$$\left(T + \frac{\partial T}{\partial x}\delta x\right)^4 \approx T^4 + 4T^3\frac{\partial T}{\partial x}\delta x \tag{21}$$

A formulation of the net heat flux ($\mathbf{q}_{\text{r}}$) in the x direction ($q_{\text{r}x}$) can be obtained as in Eq. (22).

$$q_{\text{r}x} = \mathbf{q}_{\text{A}} - \mathbf{q}_{\text{B}} = -4\sigma\varepsilon T^3\frac{\partial T}{\partial x}\delta x \tag{22}$$

In order to consider the energy variation induced by radiation on a finite control volume of dimension $dx \times dy \times dz$, one could evaluate the energy change due to radiation heat flux through the faces perpendicular to the domain plane:

$$Q_{\text{r}xy} = -\nabla\cdot\mathbf{q}_{\text{r}} = 4\sigma\varepsilon\delta_x\left[\frac{\partial}{\partial x}\left(T^3\frac{\partial T}{\partial x}\right) + \frac{\partial}{\partial y}\left(T^3\frac{\partial T}{\partial y}\right)\right] = 4\sigma\varepsilon\delta_x\nabla\cdot\left(T^3\nabla T\right) \tag{23}$$

Hence, the local 2D self-radiation heat flux expression results as shown in Eq. (24).

$$\mathbf{q}_{\text{r}} \approx -4\sigma\varepsilon\delta_x T^3\nabla T \tag{24}$$

The absorption length δ_x (or optical thickness) is assumed to be isotropic, and it has to be equal to or smaller than the smallest cell size for the numerical solution to be valid.

2.7. Vertical radiation

The vertical radiation heat loss shown in Eq. (25) [40] consists of the emission along the z direction –i.e. perpendicular to the simulated xy domain.

$$Q_{\text{r}z} = \sigma\varepsilon\delta_z^{-1}\left(T_{\text{amb}}^4 - T^4\right) \tag{25}$$

2.8. Closure equations

Finally, the system is closed with the following equations:

$$\bar{M} = \sum_{i=1}^{5} X_i M_i \tag{26}$$

$$c_\mathrm{p} = \sum_{i=1}^{5} X_i \frac{M_i}{\bar{M}} c_{\mathrm{p}i} \tag{27}$$

The *molar mass* ($\bar{M}$) of the mixture in Eq. (26) is a linear combination of the molar masses of each chemical species (M_i) multiplied by the respective mass fraction (X_i). Similarly, the total *heat capacity coefficient* at constant pressure (c_p) of the mixture in Eq. (27) is obtained by weighted summation of the partial heat capacities ($c_{\mathrm{p}i}$) of each chemical species.

3. Numerical solution

The numerical scheme used to solve the system of PDEs in Eqs. (7) and (8) is given by the 2$^{\mathrm{nd}}$ order centred finite difference method for the spatial integration and the 4$^{\mathrm{th}}$ order Runge-Kutta method (RK4) for the time integration. For example, time integration for Eq. (5) is as shown in Eq. (28), where $\tilde{T} = c_\mathrm{p} T$:

$$\begin{cases} \tilde{T}^{k+1} &= \tilde{T}^k + F_T \Delta t \\ F_T &= (1/6)\left(F_{T,1} + 2F_{T,2} + 2F_{T,3} + F_{T,4}\right) \\ F_{T,1} &= F_T\left(\tilde{T}^k, X_i^k\right) \\ F_{T,2} &= F_T\left(\tilde{T}^k + F_{T,1}\frac{\Delta t}{2}, X_i^{k+\frac{1}{2}}\right) \\ F_{T,3} &= F_T\left(\tilde{T}^k + F_{T,2}\frac{\Delta t}{2}, X_i^{k+\frac{1}{2}}\right) \\ F_{T,4} &= F_T\left(\tilde{T}^k + F_{T,3}\Delta t, X_i^{k+1}\right) \end{cases} \tag{28}$$

This is an accurate and efficient (explicit) method, although it is still conditionally stable. For instance, the maximum time-step to ensure stability for a grid-size of 0.25 m^2 is 5 s.

All numerical derivatives in space are 2$^{\mathrm{nd}}$ order accurate except for when applying the flux limiter operator in the transport term, which gradually reduces accuracy to 1$^{\mathrm{st}}$ order by using an upwind scheme.

As far as Boundary Conditions (BCs) are concerned, the main idea is to keep the simulation domain as unconstrained as possible, allowing free heat fluxes through the boundaries. Therefore, we applied Dirichlet BCs on both the temperature (ambient) and the chemicals mass fractions. The fuel mass fraction right at the boundary and some neighbouring cells is set to zero, creating a safe band where the fire cannot spread. In order to avoid eventual artificial effects on the solution due to boundary assignment, the flaming area is kept far from the domain edges.

Regarding the initial conditions, the initial temperature field is set to the atmospheric temperature at the considered altitude. The ignition point is represented by a Gaussian distribution, which peak temperature is 300 K higher than the pyrolysis temperature to avoid numerical effects related to discontinuities or excessively steep gradients. The flammable gas mixture is lean, setting the initial fuel molar fraction to 10% with the remaining 90% air, which results in an almost unlimited availability of oxygen for the combustion to take place.

A flux limiter is applied to the transport term Q_{w} in Eq. (13) in order to constrain the heat fluxes with the wind direction. The flux limiter in Eq. (29) is formulated in order to have a gradual switch from centred differences at no-wind condition towards upwind differences scheme for very strong winds.

$$Q_{\mathrm{w}} = -\rho c_{\mathrm{w}} \overline{\mathbf{u} \cdot \nabla \tilde{T}}^{FL} \tag{29}$$

Moreover, negative transport heat fluxes due to wind are reduced in order to enforce the permanence of the flame in the vegetation stratum, which is not a volatile gas mixture.

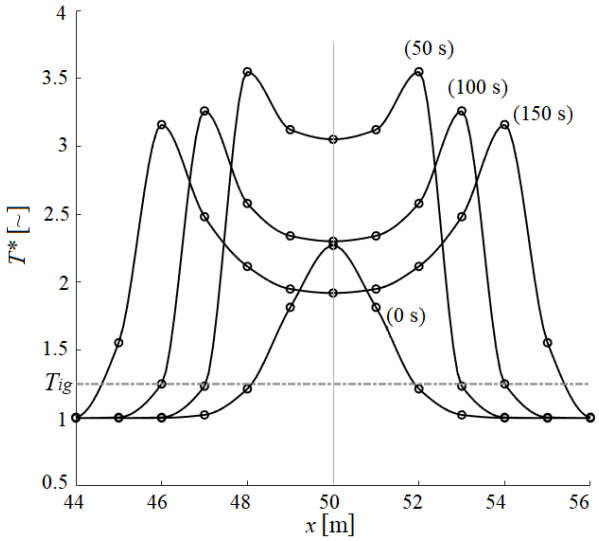

Figure 2: Temperature profile along a radial direction across an ignition point, where $T^* = T/T_{\mathrm{amb}}$.

In cases with multiple types of fuels present in the same domain, a problem arises in choosing the parameters for the spatial derivatives which affect the value of the heat fluxes at the interface between two different fuel types. Table 1 shows how we choose between the local, the minimum, and the maximum values. While it would have made sense to choose local values for δ_z^* and χ, better predictions were observed with the choices shown in Table 1.

parameter	c_{h}	A_{r}	κ	δ_x^*	δ_z^*	χ	$\mathbf{T}_{\mathrm{ig}}$	c_{w}
value	local	local	min	min	min	max	local	local

Table 1: Choice of parameters' values at the interface between two different fuels as either local, minimum or maximum.

The model's predictions have been compared against the simulated dynamics obtained by other models and experimental results from the literature. For instance, Fig. 2 shows the radial temperature profile of a circular flame growing radially from a single ignition point in a grass bed in the centre of the domain. A qualitatively and quantitatively similar result was reported by Ferragut et al. [15], whose model was previously introduced in Eq. (1) in Section 1.

Furthermore, in order to observe the combustion dynamics, we study the evolution in time of temperature, fuel mass fraction, products mass fraction (e.g. CO_2), and fuel mass loss rate. This is shown in Fig. 3, where some non-dimensional values are defined as follows:

i) Temperature:
$(T - T_{\text{amb}})^\star = (T - T_{\text{amb}})/T_{\text{amb}}$

ii) Fuel mole fraction:
$X^\star_{\text{CH}_4} = X_{\text{CH}_4}/X^{t=0}_{\text{CH}_4}$

iii) Product mole fraction:
$X^\star_{\text{CO}_2} = X_{\text{CO}_2}/X^{t\to\infty}_{\text{CO}_2}$

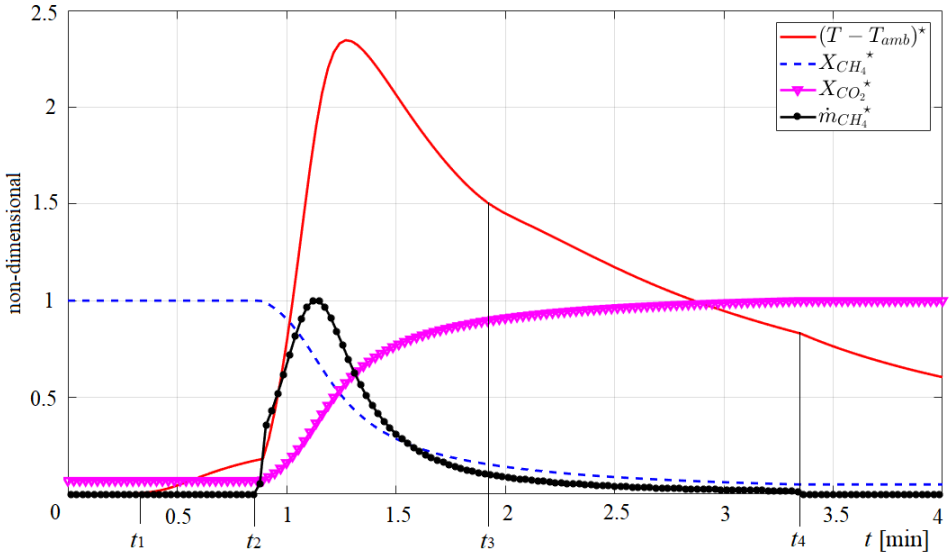

Figure 3: Ignition dynamics of a cell showing the average temperature normalised by the ambient temperature, the molar fraction of fuel by its initial value, the molar fraction of the carbon dioxide by its final value and the mass loss rate of fuel normalised by its maximum value. The specific times t_i, with i from 1 to 4, point out a crucial event of the simulated environment.

In Fig. 3, it is easy to recognise the heating phase ($t_1 < t < t_2$), combustion phase ($t_2 < t < t_4$), ignition of a neighbouring cell ($t_3 < t < t_4$), and suppression/cooling phase ($t > t_4$). The local combustion dynamics obtained with the proposed model is also qualitatively and quantitatively similar to those reported from other models and experiments such as those in [41; 42; 43].

4. Numerical experiments

Absent access to detailed wildfires databases, the proposed fire propagation model (FireProM-F) is calibrated against a commercial simulator for single-species and uniform wind scenarios. The commercial simulator of choice is FARSITE [8], as it has been validated against historical fires and is equipped with an extensive collection of fuel models. The calibrated model is then

tested for different wind speeds and on different mixed fuels scenarios, comparing results against FARSITE's predictions. Furthermore, a simple field experiment is reproduced qualitatively to demonstrate that FireProM-F is able to capture the relevant dynamics of fire front propagation. In addition, a medium-scale realistic scenario is designed for further testing, which also includes atmospheric wind and barriers to the propagation of the wildfire. Like in the previous tests, FARSITE's predictions are used for reference. Other authors have also followed the approach of using this commercial simulator to validate wildfire models (see [50]).

4.1. Model calibration

The calibration methodology adopted is described in this section, where the reference values are obtained by carrying out simulations of fire propagation especially designed for this purpose using the popular Fire Area Simulator FARSITE.

The methodology consists of starting a fire from a single ignition point within a uniform fuel bed in the centre of a square domain of 100 m × 100 m in the absence of wind, atmospheric conditions at sea level, and 20% of fuel moisture. Evidently, the fire is to propagate radially displaying a circular propagation front. The ignition point is represented by a Gaussian distribution, as dicussed in Section 3. Whilst one of the most relevant features of wildfires is the rate of spread (RoS), an indirect way to take this into account while also considering a 2D propagation is by using as a reference the burnt area (A_b) once the wildfire has propagated for a predefined length of time. As a trade-off between computational time and reliability, the fire is allowed to propagate for 10 min before extracting this reference value. Note that A_b is defined as the area that, at any time during the simulation, has had some of its fuel burning.

Thus, the objective is to minimise the error between the burnt area predicted by our model (A_b) and the one predicted by FARSITE (A_ref). The optimisation problem is formulated in Eq. (30) where $\mathbf{x}$ is a vector gathering seven calibration variables, namely: the combustion heat proportionality coefficient (c_h), the pre-exponential Arrhenius coefficient (A_r), the thermal conductivity (κ), the modified optical thickness on the simulation plane ($\delta_x^\star$), the modified optical thickness in the vertical direction ($\delta_z^\star$), the turbulent convection coefficient (χ), and the effective ignition temperature (T_ig). Calibration variables and their feasible ranges are shown in Table 2.

$$\begin{aligned} \underset{\mathbf{x}}{\text{Minimise}} \quad & (A_\mathrm{b} - A_\mathrm{ref})^2 \\ \text{Subject to} \quad & T_\mathrm{max} = T_\mathrm{ref} \\ & \mathbf{x} \in [\mathbf{x}_\mathrm{min}, \mathbf{x}_\mathrm{max}] \end{aligned} \tag{30}$$

T_ref = 1,200 K is the temperature of wood combustion in the absence of wind and crown fire [41]. Since higher temperature peaks are possible under different circumstances, this is imposed as a soft constraint by setting a small tolerance. The optimisation problem is solved using SQP, with variables calibrated for three different types of fuel. Adopting the same standard classification as FARSITE [44], these are: FM1 (short grass), FM2 (timber), and FM6 (dormant brush and hardwood slash). Resulting values of the calibrated variables are provided in Table 3.

c_h [~]	A_r [$\mathrm{K^{-1}s^{-1}}$]	κ [$\mathrm{Wm^{-1}K^{-1}}$]	δ_x^* [m]	δ_z^* [m]	χ [$\mathrm{Wm^{-3}K^{-1}}$]	T_ig [K]
$[0.7, 1.2]$	$[1, 10] \times 10^{-5}$	$[0.1, 1]$	$[1, 100] \times 10^{-2}$	$[0.1, 10]$	$[1, 10] \times 10^{-2}$	$[T_\mathrm{amb}^+$,800]

Table 2: Feasible range for calibration variables of the proposed fire propagation model.

All calibration variables in the model have physical meaning, as described below:

FM	c_h [~]	A_r [$K^{-1}s^{-1}$]	κ [$Wm^{-1}K^{-1}$]	δ_x^* [m]	δ_z^* [m]	χ [$Wm^{-3}K^{-1}$]	T_{ig} [K]
1	0.995	5.757×10^{-5}	0.978	3.43×10^{-2}	1.67	4.92×10^{-2}	374.5
2	0.988	4.324×10^{-5}	0.499	3.65×10^{-2}	1.49	5.16×10^{-2}	458.3
6	0.803	4.154×10^{-5}	0.255	2.98×10^{-2}	1.91	2.16×10^{-2}	431.6

Table 3: Variables calibrated with respect to the burnt area (A_b) predicted by FARSITE 10 min after ignition.

- c_h is a proportionality coefficient that takes into account the possibility of burning fuels that have different specific combustion energy with respect to gaseous methane. Considering the reaction in Eq. (4), the energy output due to combustion is predefined by the reference enthalpy of each chemical species involved between products and reactants, as shown in Eq. (10). In order to consider a wider spectrum of fuels that might have different reference enthalpy than that of methane, the combustion enthalpy of the gaseous mixture of methane and air is multiplied by c_h. Refer to Eq. (9).

- A_r is the pre-exponential Arrhenius coefficient, which affects the reaction rate. Similar to c_h, the reference chemical reaction is the combustion of methane that has a precise reaction rate. Therefore, in order to consider different combustion rates, A_r is a critical parameter to be calibrated. This will sensibly change the combustion power output.

- κ is the thermal conductivity, which controls the heat transferred by conduction.

- $\delta_x^\star$ is the modified optical thickness in the simulation plane as defined in Eq. (31), where δ_x is the optical thickness in x whose value depends on factors such as porosity and smoke presence, and must be smaller than the cell-size as a model assumption (see Section 2.6).

- $\delta_z^\star$ is the modified optical thickness in the vertical direction as defined in Eq. (32), where δ_z is the optical thickness in z whose value depends on the height of the vegetation stratum and on smoke presence.

- χ is the turbulent convection coefficient, which strongly depends on the combustion power strictly affecting the intensity of the buoyancy fluxes.

- T_{ig} is the effective ignition temperature, which can be far lower than the actual ignition temperature for the reference fuel (CH_4) since we are considering the average value in the cell and we are modelling wood combustion. The activation temperature T_a for the combustion to take place is set equal to T_{ig}.

$$\delta_x^\star = \varepsilon \delta_x \tag{31}$$

$$\delta_z^\star = \delta_z / \varepsilon \tag{32}$$

Note that ε in Eqs. (31)-(32) is the radiation emissivity, which depends on both porosity of the vegetation medium and smoke presence.

The calibration described thus far applies to no-wind conditions. Hence, a new calibration variable is considered to account for the wind effect, namely the wind reduction coefficient (c_w). The latter is always smaller than one, and reduces the atmospheric asymptotic wind velocity

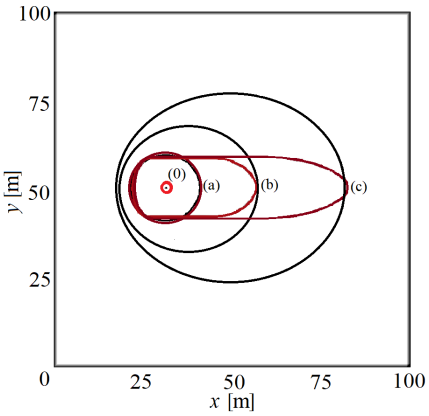

Figure 4: Fire perimeter predictions by FireProM-F (red) and by FARSITE (black) 10 min after ignition with (a) 0 m/s, (b) 5 m/s and (c) 10 m/s wind speeds blowing from left to right. The ignition point is marked as (0), and a slow-burning fuel is used.

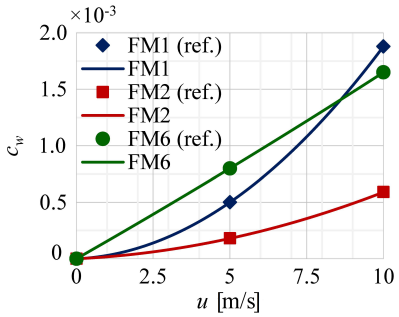

Figure 5: Wind reduction coefficient laws in relation to wind speed for three fuel types, where ♦, ■ and • are the reference calibration points.

to an effective wind velocity due to drag at the interface and inside the vegetation layer. This parameter should depend on porosity, average height, and crown coverage.

Two different wind velocities are considered, 5 m/s and 10 m/s, with the previous case of 0 m/s added as a third case scenario (no-wind). Interestingly, the shape of the fire front predicted by the proposed *physics-based model* and the one predicted by the *mechanistic surrogate model* embedded in FARSITE differ considerably for windy conditions. Therefore, it makes little sense to use A_b as the reference response. Instead, the downwind flame-front run ($\widehat{\Delta X}$) is used, and the objective function in Eq. (30) is replaced by the one in Eq. (33) for the calibration of $\boldsymbol{c}_w$.

$$\underset{c_w}{\text{Minimise}} \quad \left(\widehat{\Delta X} - \widehat{\Delta X_{\text{ref}}}\right)^2 \tag{33}$$

The fire front for each of these three scenarios is shown in Fig. 4, where the predictions made by the proposed *calibrated* physics-based model are displayed in red lines whereas those made by the commercial simulator FARSITE are displayed in black lines. As can be observed, the $\widehat{\Delta X}$ predicted by the two models coincide whereas the predicted values of the A_b show great discrepancies. In particular, FARSITE predicts significant expansions of the fire perimeter against the wind and on both flanks. This is an artificial effect introduced by the geometrical construction of the flame front based on elliptic waves with their back focuses forcibly placed on the ignition points in the fire perimeter (Huygens principle). This is a known issue associated with the embedded 2D fire growth model. It is important to note that, while the A_b depends on the elliptical growth (mechanistic surrogate) model, the size of the major axis depends only on the RoS in the direction of the wind calculated in advance in FARSITE using Rothermel's model. This supports the case for using $\widehat{\Delta X}$ rather than A_b as the reference variable for the calibration of $\boldsymbol{c}_w$.

Since aerodynamic coefficients are usually modelled proportionally to a certain power of the wind velocity [45], it is assumed here that c_w follows a quadratic law, as shown in Fig. 5. Thus, the calibrated $\boldsymbol{c}_w$ corresponding to the three wind velocities are interpolated with a quadratic polynomial for each of the three fuels considered. Fig. 5 also shows that FM1 (blue) and FM2

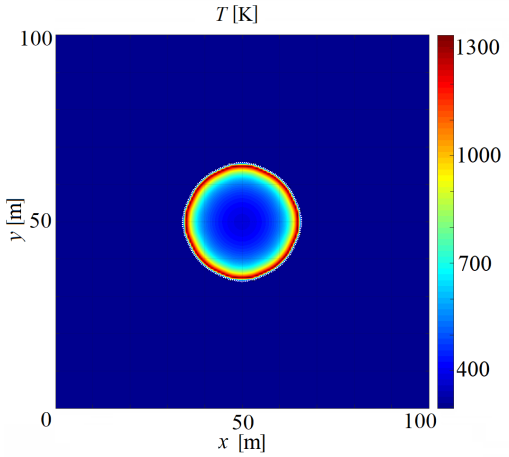

Figure 6: Temperature field 10 min after single-point ignition of FM1 fuel bed under no-wind condition.

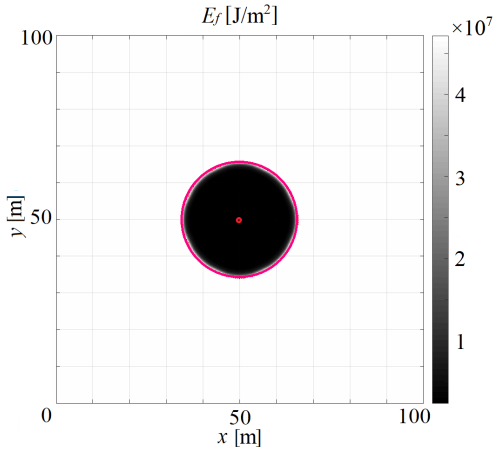

Figure 7: Energy fuel field 10 min after single-point ignition of FM1 fuel bed under no-wind condition. The non-white region shows the burnt area (A_b), the red dot shows the ignition point, and the red circle shows the fire perimeter predicted by FARSITE.

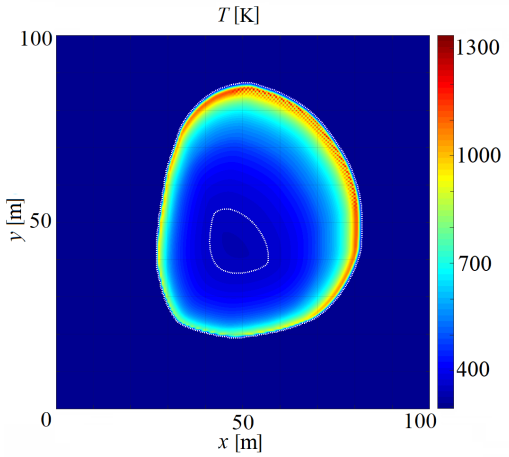

Figure 8: Temperature field 10 min after single-point ignition of FM1 fuel bed with 10 m/s wind. The inner contour encloses a region with $T < T_{ig}$.

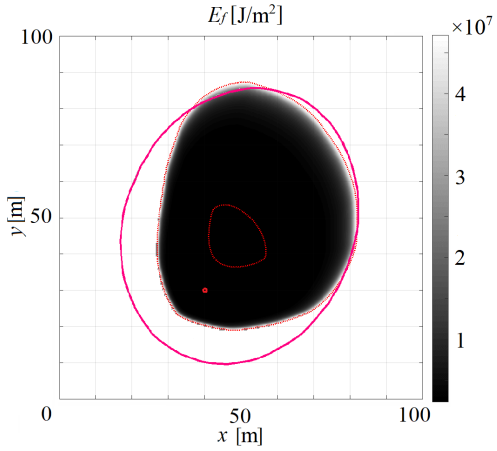

Figure 9: Energy fuel field 10 min after single-point ignition of FM1 fuel bed with 10 m/s wind. The non-white region shows the burnt area (A_b), the red dot shows the ignition point, and the red ellipse shows the fire perimeter predicted by FARSITE. The inner contour encloses a region with $T < T_{ig}$.

(red) follow marked parabolic trends whereas FM6 (green) displays an almost linear one. This is because FM6 consists of bushes with foliage which, despite being very flammable, are coarse. Hence fire propagation is strongly driven by wind, which can almost freely penetrate the highly porous media somewhat justifying the quasi-linear trend of c_w.

Two examples of fire spread from a single source predicted by the calibrated model are shown

in Figs. 6–9 for fuel FM1 uniformly distributed in the domain. Figs. 6 and 7 show the temperature and fuel energy fields, respectively, for the no-wind case whereas Figs. 8 and 9 show them for a 10 m/s wind. Note that any non-white region in the fuel energy field contributes to the total A_b. The outer solid red lines in Figs. 7 and 9 are the fire perimeters modelled by FARSITE. Clearly, agreement is almost perfect for the no-wind case and deteriorates once wind is introduced, as previously discussed. The inner dotted contours in Figs. 8 and 9 enclose regions with $T < T_{ig}$.

4.2. Model tests

In order to test the proposed FireProM-F beyond the calibration scenarios, two sets of numerical experiments are carried out in this section: one for different wind speeds, and the other for different inhomogeneous fuel mixtures. Predicted fire perimeters are compared against those modelled by FARSITE, and the satisfaction of the soft T_{max} constraint is checked.

4.2.1. Tests under different wind speeds

The first set of experiments consists of testing the calibration curves in Fig. 5 to set the c_w coefficient in the transport term in Eqs. (7) and (13) as a function of the wind velocity. Thus, wind velocities were selected within the calibration range [0 m/s–10 m/s], but also outside by extrapolating the curves up to 15 m/s. We believe that the parabolic formulation of c_w would still work for stronger winds, though this has not been tested here.

As shown in Figs. 10, 11 and 12, the discrepancies in the predictions of the fire-front runs ($\widehat{\Delta X}$) by our calibrated model and FARSITE are smaller than 5% for each of the three fuels, even for wind velocities larger than 10 m/s. This calibration may also be applied to the remaining standard fuels described by Anderson [44].

4.2.2. Tests under different fuel mixtures

While the model has been calibrated for individual fuels, the aim here is to test its predictions for a mixture of them. Thus, the three different fuel types have been allocated randomly throughout the domain in order to simulate a plausible inhomogeneous distribution of fuel energy. The fuels are mixed randomly but predefining their occupational percentages (C_{FM1}, C_{FM2} and C_{FM6}), with each cell containing only one type of fuel. Tests are performed for two ignition cases: single-point ignition in the centre of the domain (as during calibration), and multiple ignitions from four sources. An example of the fire propagation when mixing the three fuel models in equal percentages and for a fire initiated from four ignition points is shown Figs. 13 and 14. Since calibration was performed for reference values extracted 10 min after ignition, simulations are carried out for an extended period of 20 min to confirm that the agreement persists.

As can be observed in Figs. 13 and 14, the predictions of the fire perimeter by our calibrated model and by FARSITE are in clear agreement. Also note that the maximum temperature in the field is around the value set for T_{max} during calibration (1,200 K).

Percentage errors (ϵ) for pairwise mixtures of the three fuels in different occupational percentages are shown in Figs. 15, 16, and 17. It was expected that ϵ for the mixture would monotonically vary between the values at the two extremes with single fuel, e.g. along the red lines in the figures. However, the discrepancies between the predictions of the A_b increase when mixing fuels, even if there is some skewness towards the fuel with higher ϵ. We believe this to be caused by a different modelling of the fire propagation in the neighbourhood of an interface between two different fuels. For instance, FARSITE averages the properties of the fuels traversed by the fire front during the time-step considered [8; 46], whereas FireProM-F chooses the parameters

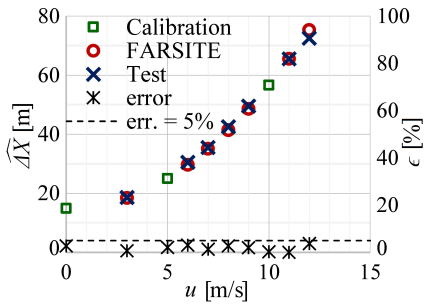

Figure 10: Fire-front run $\widehat{\Delta X}$ predicted by our model and by FARSITE, and their difference (error), for a range of wind velocities and FM1

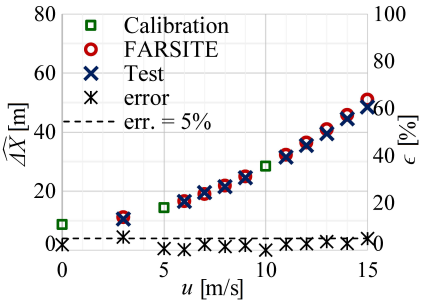

Figure 11: Fire-front run $\widehat{\Delta X}$ predicted by our model and by FARSITE, and their difference (error), for a range of wind velocities and FM2

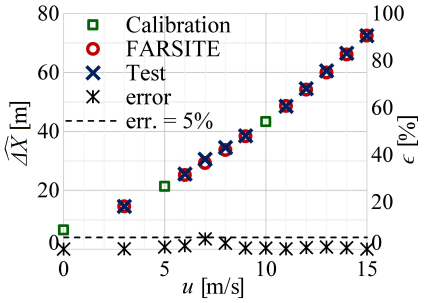

Figure 12: Fire-front run $\widehat{\Delta X}$ predicted by our model and by FARSITE, and their difference (error), for a range of wind velocities and FM6

as previously explained in Table 1. Nonetheless, discrepancies of predictions are consistently maintained below 5% for different mixtures of fuels.

Analysing the performance of the model for cases with multiple ignitions, a 3% increment of ϵ is observed for a fire originating from four ignition points when compared to one propagating from a single source. This may be –at least partially– due to the geometrical formulation of the fire front in FARSITE, as marker methods are known to have difficulties in handling situations such as when the edges of a concave fire front –or two separate fire fronts– collide. With the current crossover management algorithm, the superposed area is simply eliminated disregarding the energy that theoretically has been generated in producing it. Furthermore, in cases of junction fires and concave fire fronts, experiments show that the RoS should momentarily increase and then gradually slow down to reach normal speed once the shape becomes convex [47]. As opposed to FARSITE, FireProM-F appears to reproduce this phenomenon to some extent.

4.3. Reproducing real fire experiments

In this section, the predictions of FireProM-F are qualitatively compared against well established historical experiments [48; 49] in terms of the shape of the fire front. The reference field experiments were performed on 100×100 m^2 lots with different kind of grass fuels for characterisation. Some properties are the burning rate, the RoS, susceptibility to wind, and flame

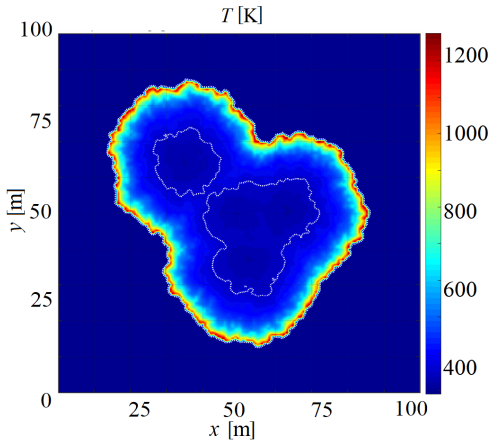

Figure 13: Temperature field 20 min after multiple ignition of a randomly mixed fuel bed with equal partition of FM1, FM2 and FM6. The inner contour encloses a region with $T < T_{ig}$.

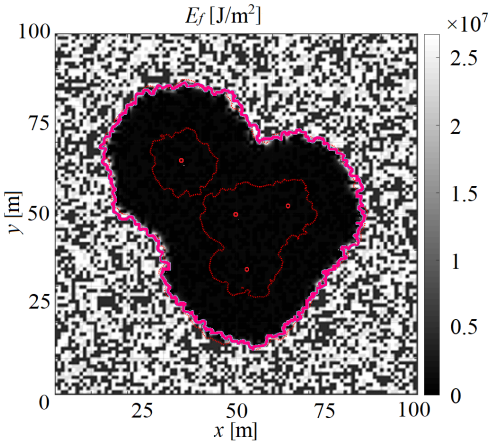

Figure 14: Fuel energy field and fire perimeter 20 min after multiple ignition (red dots) of a randomly mixed fuel bed with equal partition of FM1, FM2 and FM6. The uniform dark region with low density of fuel energy depicts the A_b predicted by FireProM-F whereas the red contour is FARSITE's prediction of the fire perimeter. The inner contour encloses a region with $T < T_{ig}$.

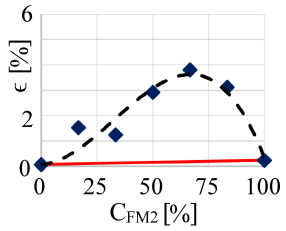

Figure 15: Estimation error distribution for different percentages of two randomly mixed fuel types: FM1 and FM2. In continuous line the expected trend. At 0% of FM2 corresponds 100% FM1.

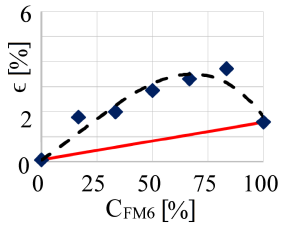

Figure 16: Estimation error distribution for different percentages of two randomly mixed fuel types: FM2 and FM6. In continuous line the expected trend. At 0% of FM6 corresponds 100% FM1.

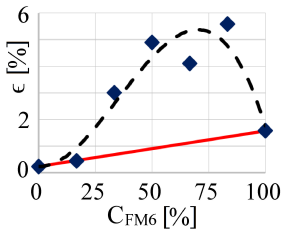

Figure 17: Estimation error distribution for different percentages of two randomly mixed fuel types: FM1 and FM6. In continuous line the expected trend. At 0% of FM6 corresponds 100% FM2.

intensity. Since FireProM-F has not yet been calibrated for a wide variety of fuels, other features such as the RoS are not considered here. The experiments in [48; 49] are as follows:

1. Using torches, two persons ignite one edge of the fuel bed (west in Fig. 4 in [48]), starting from the centre of the edge and walking apart from each other towards the vertices.
2. Wind blows from west to east, making the forming fire front assume a Gaussian shape.
3. This evolves into a triangular shape due to larger heat transport towards convex areas.
4. The fire front eventually takes rounded shapes, from a tear-drop to a final parabolic shape.

As shown in Fig. 18, FireProM-F is able to predict this behaviour. Thus, label (a) shows a Gaussian shape of the fire front after 48 s, label (b) shows a triangular shape after 114 s, label (c) shows a tear-drop shape after 301 s, and finally a parabolic fire front can be observed at 538 s.

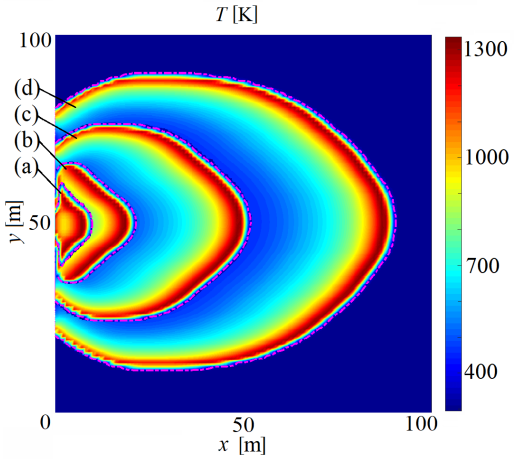

Figure 18: Temperature field after dynamic linear ignition on the west side of a 100×100 m^2 field with uniformly distributed FM1 fuel traversed by a 10 m/s horizontal wind. The figure shows a composite temperature colourmap and corresponding fire front (dotted magenta line) built from snapshots at four different times. The fire front takes a *Gaussian* shape at 48 s (a), a *triangular* shape at 114 s (b), a *tear-drop* shape at 301 s (c), and a parabolic shape at 538 s (d).

4.4. Simulation under realistic scenario

This section aims to simulate the fire propagation over a realistic large-scale scenario in order to demonstrate the reliability of the predictions made by the proposed FireProM-F. The realistic scenario consists of a square lot of forest of 1500×1500 m^2 extracted from a tutorial example provided by FARSITE. Topographic maps like this one are usually provided by the Geographic Information System (GIS), and can provide information about the vegetation cover and type. The lot, shown in Fig. 19, comprises fuels FM1, FM2 and FM6, as well as an obstacle through which the fire is not allowed to propagate but the wind may cut through unaffected. Such an obstacle may be given by a natural barrier like a lake or rocks. It is important to note that the precision of the vegetation raster provided by the GIS ($\approx$ 30 m) is not the same as the cell-size used in our simulations (1 m^2). Slope and elevation are set to flat and sea-level conditions, as our model does not yet include these features. Moisture level is set to 20% as during calibration.

Two experiments are carried out for a wildfire propagating from a single ignition point, one under no-wind condition and the other with a 5 m/s wind blowing at a 60° angle. The temperature field after 3 hrs of propagation for the first experiment is shown in Fig. 20, where the flame front is displayed by the outer dotted white contour. The inner white contour encloses a region with $T < T_{\mathrm{ig}}$. The fire front predicted by FARSITE is not displayed because it overlaps almost exactly with the one predicted by FireProM-F. For the second experiment, the temperature field after 3 hrs of propagation is shown in Fig. 21, where the meaning of the dotted white contours is the same as in the first experiment. However, the fire perimeter predicted by FARSITE is now displayed in a solid magenta contour. Predictions in this case are not perfectly overlapping but still appreciably similar.

It is interesting to notice from Figs. 20 and 21 that certain areas within the field are observed to retain higher temperatures than neighbouring areas. If these figures are analysed in conjunction with Fig. 19, it can be inferred that these areas correspond to the most energetic fuels, namely FM2 and FM6, which are harder to be ignited but provide more energy. All things considered, the results from the two experiments are satisfactory, fulfilling our expectations.

In Table 4 the computational times for different domain sizes are collected. It can be noticed that for a fairly large domain of 1 hectare the simulation is faster than real time. The turning point when the run time and the simulation time are identical is about 4 hectares.

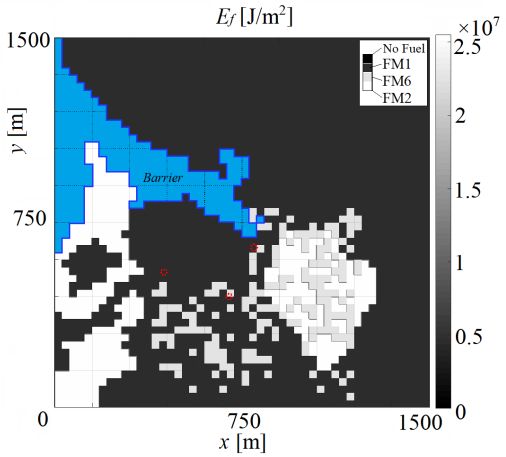

Figure 19: Fuel energy field over a 1500×1500 m^2 wildland lot. The blue area represents a barrier to the fire propagation (e.g. a lake) while the grey scale represents the fuel energy. There are three fuel types, namely FM1 (0.49×10^7 J/m^2), FM2 (2.67×10^7 J/m^2) and FM6 (2.34×10^7 J/m^2). Initial flame contour shown in red.

Domain size [m^2]	N [$\times 10^3$]	**Simulation time** [h]	**Run time** [h]	**Ratio** [~]
100×100	10	0.33	0.25	0.75
600×600	360	2.00	3.00	1.50
1500×1500	2250	3.00	28.00	9.33

Table 4: Computational time for different domain sizes (N number of points) performed with $\Delta x = 1$ m and $\Delta t = 10$ s, using Matlab R2017a on a Windows machine with an Intel Xeon CPU @3.20 GHz

4.5. Discussion of results

Despite a number of simplifying assumptions aimed at making the model fast to simulate, the underlying physics appear to be comprehensive enough to capture the major phenomena that govern the behaviour of real fires. As a first step towards validation, eight parameters with physical meaning were calibrated within realistic ranges using FARSITE simulator to generate reference values, as this widely used commercial simulator has been shown to reliably reproduce historical fires. To this end, seven parameters were calibrated to match the burnt area and one to match the downwind fire front run for three different uniform fuels and three wind speeds.

Several numerical experiments were carried out to test the calibrated model, including one in a medium-scale realistic scenario with mixed fuels, natural barrier, and atmospheric wind.

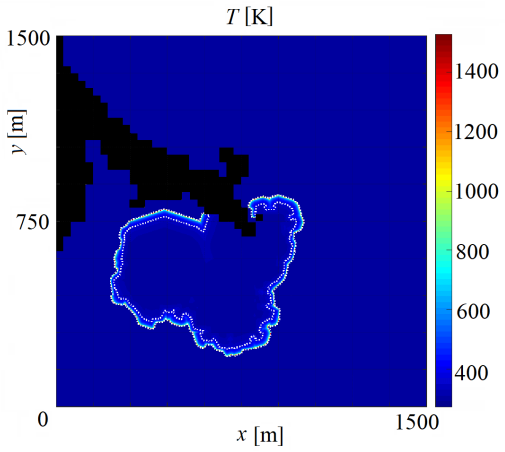

Figure 20: Temperature field 3 h after three-point ignition (see Fig. 19 for their location) under no-wind condition. The outer dotted white contour displays the fire front whilst the inner one encloses a region with $T < T_{ig}$.

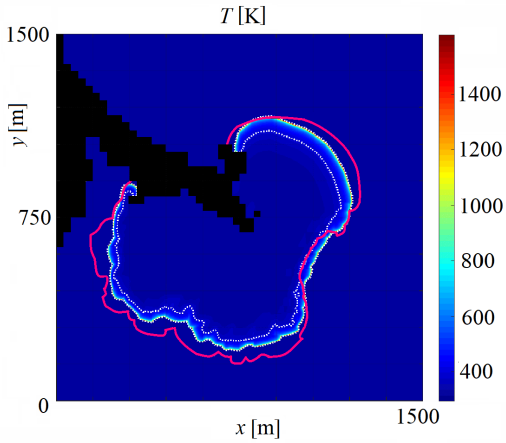

Figure 21: Temperature field 3 h after three-point ignition and 5 m/s wind. The outer dotted white contour displays the fire front whilst the inner one encloses a region with $T < T_{ig}$. The magenta contour is the fire front predicted by FARSITE.

The fire perimeters predicted by FireProM-F and by FARSITE simulator showed nearly perfect agreement for no-wind conditions. Agreement deteriorated once wind was introduced, especially in terms of rates of spread (RoS) against the wind and on the flanks. This is likely to be due to the elliptical growth geometrical approach adopted by FARSITE, which is believed to overestimate the RoS in those directions.

In addition, a field experiment was qualitatively reproduced using FireProM-F, demonstrating its ability to predict the same shapes of the fire fronts as the real fire.

Overall, the numerical experiments showed that FireProM-F is able to produce fast and reliable predictions of the fire perimeter, with the added benefit of being physics-based. For a grid of $4{\times}10^4$ points on a standard computer with Intel Xeon CPU (@3.20 GHz), FireProM-F simulates 1 min of fire dynamics in about 58 s (faster than real-time). For larger-scale experiments, the computational effort required is evidently higher so the simulations are slower than real-time.

5. Conclusions

Wildfires are dangerous uncontrolled phenomena which can have devastating health, social, economic and environmental impacts. Their frequency and severity have progressively increased for decades. Therefore, the development of tools to support the management of wildfires is gaining interest as this becomes an increasingly pressing issue worldwide.

Traditionally, fire propagation models were aimed either at the development of fire danger rating systems or at the accurate quantification of wildfire events [1]. We propose that their use be extended to two new crucial applications: 1) simulation-based testing of fire management and suppression technologies; and 2) integration into fire suppression technologies as a predictive tool to support autonomous decision-making.

Advanced physics-based models which incorporate a wide range of fire dynamics phenomena such as FDS [13] are computationally intensive and cannot be used in real time. In turn,

operational fire spread models such as FARSITE [8] are useful as real-time management tools, but they are not physics-based. This paper presented the mathematical formulation, numerical solution, calibration and testing of a physics-based **Fire Pro**pagation **M**odel for **F**ast simulations (FireProM-F) in two-dimensional space. A major motivation is to support the design of innovative fire management and suppression technologies and strategies, as well as to function as a decision-support tool to assist firefighters in the use of current technology. Hence the need for the model to be physics-based and computationally inexpensive: the modelling of interactions between fire and suppressant must be possible, and simulations must be in real-time or faster.

In addition, the use of autonomous technologies to operate in hazardous environments such as wildfires are currently gathering momentum and gaining interest from researchers and practitioners. For instance, Innocente and Grasso [5] propose the use of self-organising swarms of drones for autonomous firefighting. These types of technologies require models like FireProM-F for their development and extensive testing. Furthermore, a faster-than-real time model may also be used as a predictive tool to enable more advanced autonomous firefighting strategies.

References

[1] G. Perry, Current approaches to modelling the spread of wildland fire: a review, Progress in Physical Geography 22 (2) (1998) 222–245.

[2] A. L. Sullivan, Wildland surface fire spread modelling, 1990–2007. 1: Physical and quasi-physical models, International Journal of Wildland Fire 18 (4) (2009) 349.

[3] A. L. Sullivan, Wildland surface fire spread modelling, 1990–2007. 2: Empirical and quasi-empirical models, International Journal of Wildland Fire 18 (4) (2009) 369.

[4] A. L. Sullivan, Wildland surface fire spread modelling, 1990–2007. 3: Simulation and mathematical analogue models, International Journal of Wildland Fire 18 (4) (2009) 387.

[5] M. S. Innocente, P. Grasso, Self-organising swarms of firefighting drones: Harnessing the power of collective intelligence in decentralised multi-robot systems, Journal of Computational Science 34 (2019) 80–101.

[6] R. C. Rothermel, A mathematical model for predicting fire spread in wildland fuels.

[7] P. L. Andrews, Current status and future needs of the BehavePlus fire modeling system, International Journal of Wildland Fire 23 (1) (2014) 21.

[8] M. A. Finney, Farsite: Fire area simulator-model development and evaluation (1998).

[9] P. L. Andrews, The rothermel surface fire spread model and associated developments: A comprehensive explanation, Gen. Tech. Rep. RMRS-GTR-371. Fort Collins, CO: US Department of Agriculture, Forest Service, Rocky Mountain Research Station. 121 p. 371.

[10] R. Linn, A transport model for prediction of wildfire behavior, Tech. rep. (jul 1997).

[11] R. Linn, J. Reisner, J. J. Colman, J. Winterkamp, Studying wildfire behavior using FIRETEC, International Journal of Wildland Fire 11 (4) (2002) 233.

[12] O. Séro-Guillaume, J. Margerit, Modelling forest fires. part I: a complete set of equations derived by extended irreversible thermodynamics, International Journal of Heat and Mass Transfer 45 (8) (2002) 1705–1722.

[13] K. B. McGrattan, Fire dynamics simulator technical reference guide volume 1: Mathematical model [6th ed.], Tech. rep., VTT & NIST (2006).

[14] W. Mell, M. A. Jenkins, J. Gould, P. Cheney, A physics-based approach to modelling grassland fires, International Journal of Wildland Fire 16 (1) (2007) 1.

[15] L. Ferragut, M. Asensio, S. Monedero, A numerical method for solving convection–reaction–diffusion multivalued equations in fire spread modelling, Advances in Engineering Software 38 (6) (2007) 366–371.

[16] J. Margerit, O. Séro-Guillaume, Modelling forest fires. part II: reduction to two-dimensional models and simulation of propagation, International Journal of Heat and Mass Transfer 45 (8) (2002) 1723–1737.

[17] P. Grasso, M. S. Innocente, A two-dimensional reaction-advection-diffusion model of the spread of fire in wildlands, in: Advances in forest fire research 2018, Imprensa da Universidade de Coimbra, 2018, pp. 334–342.

[18] O. Séro-Guillaume, S. Ramezani, J. Margerit, D. Calogine, On large scale forest fires propagation models, International Journal of Thermal Sciences 47 (6) (2008) 680–694.

[19] V. G. Ntinas, B. E. Moutafis, G. A. Trunfio, G. C. Sirakoulis, Parallel fuzzy cellular automata for data-driven simulation of wildfire spreading, Journal of Computational Science 21 (2017) 469–485.

[20] L. H. Encinas, S. H. White, A. M. del Rey, G. R. Sánchez, Modelling forest fire spread using hexagonal cellular automata, Applied Mathematical Modelling 31 (6) (2007) 1213–1227.

[21] C. Li, J. Li, L. Hu, D. Hou, Visualization and simulation model of underground mine fire disaster based on cellular automata, Applied Mathematical Modelling 39 (15) (2015) 4351–4364.
[22] X. Rui, S. Hui, X. Yu, G. Zhang, B. Wu, Forest fire spread simulation algorithm based on cellular automata, Natural Hazards 91 (1) (2017) 309–319.
[23] N. Fernandez-Anez, K. Christensen, G. Rein, Two-dimensional model of smouldering combustion using multi-layer cellular automaton: The role of ignition location and direction of airflow, Fire Safety Journal 91 (2017) 243–251.
[24] R. M. Almeida, E. E. N. Macau, Stochastic cellular automata model for wildland fire spread dynamics, Journal of Physics: Conference Series 285 (2011) 012038.
[25] H. Gazmeh, A. Alesheikh, . M. Karimi 1, A new methodology in modeling forest fire spread using cellular automata, Journal of Advanced Science and Engineering Research.
[26] K. Yamamoto, N. Takada, M. Misawa, Combustion simulation with lattice boltzmann method in a three-dimensional porous structure, Proceedings of the Combustion Institute 30 (1) (2005) 1509–1515.
[27] B. Porterie, N. Zekri, J.-P. Clerc, J.-C. Loraud, Modeling forest fire spread and spotting process with small world networks, Combustion and Flame 149 (1-2) (2007) 63–78.
[28] A. Kacem, C. Lallemand, N. Giraud, M. Mense, M. D. Gennaro, Y. Pizzo, J.-C. Loraud, P. Boulet, B. Porterie, A small-world network model for the simulation of fire spread onboard naval vessels, Fire Safety Journal 91 (2017) 441–450.
[29] S. Osher, J. A. Sethian, Fronts propagating with curvature-dependent speed: Algorithms based on hamilton-jacobi formulations, Journal of Computational Physics 79 (1) (1988) 12–49.
[30] V. Mallet, D. Keyes, F. Fendell, Modeling wildland fire propagation with level set methods, Computers & Mathematics with Applications 57 (7) (2009) 1089–1101.
[31] A. S. Bova, W. E. Mell, C. M. Hoffman, A comparison of level set and marker methods for the simulation of wildland fire front propagation, International Journal of Wildland Fire 25 (2) (2016) 229.
[32] C. Tymstra, Development and structure of prometheus : the canadian wildland fire growth simulation model, Information report NOR-X-417, Canada Natural Resources Canada. Canadian Forest Service. (2010).
[33] K. Tolhurst, B. Shields, D. Chong, Phoenix: development and application of a bushfire risk management tool., The Australian Journal of Emergency Management.
[34] G. D. Papadopoulos, F.-N. Pavlidou, A comparative review on wildfire simulators, IEEE Systems Journal 5 (2) (2011) 233–243.
[35] K. B. McGrattan, G. P. Forney, Fire dynamics simulator user's guide (version 4), Tech. rep., VTT & NIST (2004).
[36] B. J. Mcbride, S. Gordon, M. A. Reno, Coefficients for calculating thermodynamic and transport properties of individual species, Tech. rep., NASA (1993).
[37] K. Ragland, D. Aerts, A. Baker, Properties of wood for combustion analysis, Bioresource Technology 37 (2) (1991) 161–168.
[38] A. W. Cook, Enthalpy diffusion in multicomponent flows, Physics of Fluids 21 (5) (2009) 055109.
[39] S. Mathur, S. C. Saxena, Relations between thermal conductivity and diffusion coefficients of pure and mixed polyatomic gases, Proceedings of the Physical Society 89 (3) (1966) 753.
[40] J. R. Howell, R. Siegel, M. P. Menguc, Thermal Radiation Heat Transfer, Taylor & Francis Inc, 2015.
[41] M. E. Houssami, A. Lamorlette, D. Morvan, R. M. Hadden, A. Simeoni, Framework for submodel improvement in wildfire modeling, Combustion and Flame 190 (2018) 12–24.
[42] C. Bruch, B. Peters, T. Nussbaumer, Modelling wood combustion under fixed bed conditions, Fuel 82 (6) (2003) 729–738.
[43] W. Mell, A. Maranghides, R. McDermott, S. L. Manzello, Numerical simulation and experiments of burning douglas fir trees, Combustion and Flame 156 (10) (2009) 2023–2041.
[44] H. E. Anderson, Aids to determining fuel models for estimating fire behavior, Tech. rep., USDA For. Serv. Gen. Tech. Rep. INT-122 (1982).
[45] J. Anderson, Fundamentals of Aerodynamics (Mcgraw-hill Series in Aeronautical And Aerospace Engineering), McGraw-Hill Science/Engineering/Math, 2005.
[46] R. Martin, Fire rate of spread calculation for two fuels, Western Journal of Applied Forestry 3 (2) (1988) 54–55.
[47] D. X. Viegas, J. R. Raposo, D. A. Davim, C. G. Rossa, Study of the jump fire produced by the interaction of two oblique fire fronts. part 1. analytical model and validation with no-slope laboratory experiments, International Journal of Wildland Fire 21 (7) (2012) 843.
[48] N. Cheney, J. Gould, W. Catchpole, The influence of fuel, weather and fire shape variables on fire-spread in grasslands, International Journal of Wildland Fire 3 (1) (1993) 31.
[49] N. Cheney, J. Gould, Fire growth in grassland fuels, International Journal of Wildland Fire 5 (4) (1995) 237.
[50] F. Gu, X. Hu, L. Ntaimo, Towards validation of DEVS-FIRE wildfire simulation model (2008).
URL `http://dl.acm.org/citation.cfm?id=1400549.1400603`